aerospace

MDPI

Article

Improvement of a Free-Wake Model for the Aerodynamic and Aeroacoustic Analysis of a Small-Scale Two-Bladed Propeller in Hover

Manuel Iannotta [1], Antonio Visingardi [2], Domenico Quagliarella [2], Fabrizio De Gregorio [2], Mattia Barbarino [2] and Alex Zanotti [1,*]

[1] Dipartimento di Scienze e Tecnologie Aerospaziali, Politecnico di Milano, Via La Masa 34, 20156 Milan, Italy; manuel.iannotta@mail.polimi.it
[2] Centro Italiano Ricerche Aerospaziali, Via Maiorise, 81043 Capua, Italy; a.visingardi@cira.it (A.V.); d.quagliarella@cira.it (D.Q.); f.degregorio@cira.it (F.D.G.); m.barbarino@cira.it (M.B.)
* Correspondence: alex.zanotti@polimi.it

Abstract: The aim of the present work is the improvement of a free-wake model for the analysis of a small-scale two-bladed propeller in hover. The simulations are carried out using a BEM approach implemented in the medium-fidelity solver RAMSYS. An acoustic validation is also performed using the developed tool ACO-FWH. The work proves that even mild discrepancies in the propeller geometry must be accounted for as their influence is not negligible, especially on the aeroacoustics of the propeller. In particular, the proper modeling of the blades enables the correct identification of the sub-harmonics of the SPL spectra. An optimization procedure based on the application of the evolutionary Genetic Algorithm is followed to identify the values of the parameters describing the dissipative and diffusive properties in the Bhagwat–Leishman vortex core model, an upgraded version of the classical Lamb–Oseen one. On average, this approach enabled the further improvement of the accuracy of the numerical model in terms of acoustic signature evaluation with respect to the one obtained by only modeling blade dissimilarities. The results obtained demonstrate the promising capabilities of a fine-tuned free-wake medium-fidelity approach to simulate the aerodynamic and acoustic details of a small-scale propeller in hover, provided the accurate geometrical modeling of the propeller and the selection of suitable parameters to be used in the wake modeling.

Keywords: aeroacoustics; aerodynamics; propeller; eVTOL; free-wake models; PIV

Academic Editors: Kung-Ming Chung, Tze How New, Desmond H. Lim and Nick Zang

Received: 18 November 2024
Revised: 16 December 2024
Accepted: 24 December 2024
Published: 25 December 2024

Citation: Iannotta, M.; Visingardi, A.; Quagliarella, D.; De Gregorio, F.; Barbarino, M.; Zanotti, A. Improvement of a Free-Wake Model for the Aerodynamic and Aeroacoustic Analysis of a Small-Scale Two-Bladed Propeller in Hover. *Aerospace* **2025**, *12*, 5. https://doi.org/10.3390/aerospace12010005

1. Introduction

Urban Air Mobility is, according to the EASA definition, an air-transportation system for passengers and cargo in and around urban environments. The main reason for the introduction of this innovative means of transportation lies in the fact that, according to recent projections of the United Nations, a global population of 10 billion people is estimated by 2050, 70% of which will be living in big, highly congested cities. Cities and metropolitan areas are already today powerhouses of economic growth, contributing about 60% of global gross domestic product (GDP), but they also account for about 70% of global carbon emissions and over 60% of resource use, thus representing a threat to a sustainable way of life. Therefore, UAM aims to overcome these problems by making use of the largely untapped low-altitude air space above urban landscapes and using multirotor aircraft equipped with electric propulsion (eVTOLs) that are safer, cleaner, and quieter than conventional engines.

In particular, according to EASA [1], the sustainability and social acceptance of UAM are strongly influenced by the noise generated by eVTOLs in and around the urban areas. Due to the regulations, the noise produced by flights over cities is requested to be below safety values. Therefore, its reduction becomes the most relevant constraint for the progress of this novel technology. This is the reason why, in recent years, several works, both experimental, numerical, and analytical, have been developed aimed at understanding noise pollution mechanisms related to multi-propeller systems. Full size tests are not always possible and could require a very high effort. Moreover, the investigation of scaled models in anechoic chambers or wind tunnels under monitored and controlled conditions was considered a valuable tool also for the validation of numerical simulation software.

Among the many European initiatives aimed at investigating aerodynamics and aeroacoustics of eVTOL configurations, the Group for Aeronautical Research and Technology in Europe (GARTEUR) Rotorcraft (RC) Group of Responsable, has promoted in the recent past studies related to the interactional aerodynamics and aeroacoustics of multirotor configurations. Partners from European industries, research centers, SMEs, and universities have setup consortia to put together their resources and facilities to carry out numerical and experimental research activities. In particular, the activities conducted in the GARTEUR Action Group RC/AG-26 "Noise Radiation and Propagation for Multirotor System Configurations" were devoted to the study of noise footprint related to multirotor configurations aimed at providing a comprehensive experimental database over different configurations of multi-propellers contributed by the partners. In this framework, an experimental campaign was conducted by DLR and CIRA [2] on small-scale two-bladed propellers in hover, both in isolated conditions and in tandem and co-axial configurations. The resulting database, used by the consortium to validate partners' computational tools with different levels of fidelity, is used in the present work to provide evidence of the improvements brought to the applied free-wake model.

The aim of present work is to setup and propose a methodological approach to improve the numerical simulation of the aerodynamic behavior of the isolated benchmark propeller using a medium-fidelity method. Two aspects are investigated in particular:

1. Propeller geometry: The propeller posed some difficulties in the medium-fidelity simulations carried out in the AG-26. A closer exam of the geometry, related these problems to some geometrical differences between the two blades resulting from inaccuracies in the manufacturing process. Indeed, although all the numerical aerodynamic investigations conducted by the partners were able to correlate properly with the experimental results, discrepancies appeared instead with the aeroacoustic analysis. In particular, the simulations conducted using CFD methods provided reliable aeroacoustic results, but medium-fidelity methods did not [3]. The reason for this outcome was found in the procedure that is usually adopted to mesh the propeller geometry. The volume grids used in CFD calculations are generated directly starting from the CAD file of the geometry. In this specific case, the propeller CAD file was composed of a single body. Instead, medium-fidelity solvers need to mesh just the surface of the blades and usually do not model the hub. For this reason, the blades are seen as separate entities. Since, usually, the blades of a generic rotor should be the same, it is common practice to generate the mesh on one blade only and then replicate it for as many blades as those composing the rotor. Once the dissimilarity between the two blades, they were modeled in the simulations performed in the present work as two separate bodies, each with its own real geometry, to understand if the differences found in the partners' numerical results during the AG-26 activities were produced by the geometrical inequality of the blades or by a limit in the simulation methodologies applied.

2. Vortex core model: A free-wake methodology was used in this work. The wake and vortex characteristics were modeled and tuned by means of a set of parameters. Their values and ranges have been investigated in the literature, mainly for cases related to helicopters. The present work aims at identifying, in an automatic way, the correct values of these parameters when the investigations are related to small-scale propellers.

Over recent years, advancements in High-Performance Computing (HPC) and computational methodologies have made the use of automated approaches possible for the improvement of numerical simulations. More specifically, an optimization procedure was built in the present work to evaluate the parameters used in the free-wake vortex core model applied in the medium-fidelity aerodynamic solver RAMSYS [4] in order to improve the simulation of the aerodynamic behavior of small-scale propellers. Finally, as a final validation step, the effects of the aerodynamic improvements to aeroacoustics are evaluated.

2. Materials and Methods

2.1. Propeller Geometry

The commercial Xoar-13x7 PJN wooden two-bladed propeller [5] was used for the investigations described in the present work. The related CAD geometry was produced by DLR via a 3D scan of the original propeller (see Figure 1).

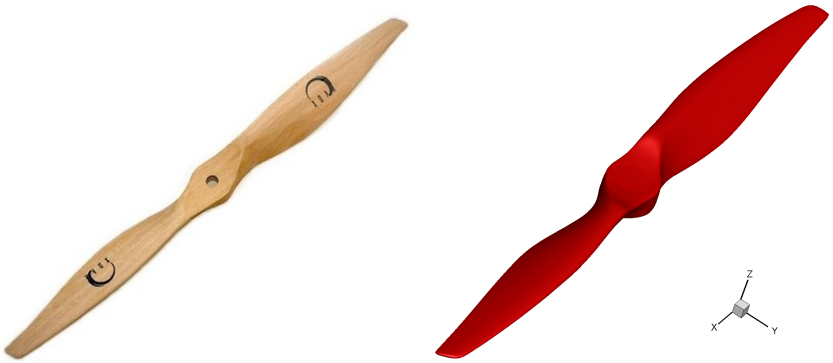

Figure 1. Original and 3D CAD scan of the Xoar-13x7 PJN propeller.

Figure 2 illustrates the blade chord, twist, and thickness distribution along the span for the reference blade, indicated in the following as Blade A. The propeller has a radius of 0.165 m and an average chord length c equal to 0.0187 m. The solidity σ is equal to 0.072.

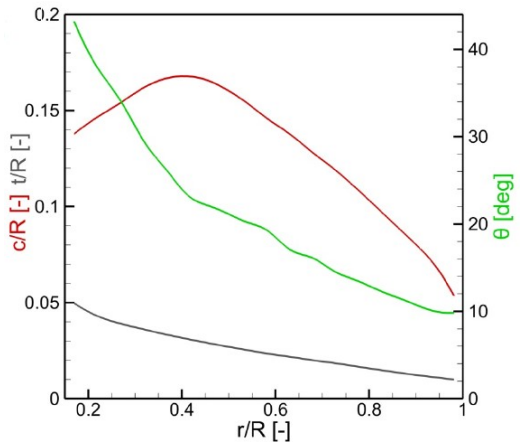

Figure 2. Chord, Twist and Thickness Spanwise Distribution for reference Blade A.

A detailed analysis of the propeller CAD file highlighted manufacturing inaccuracies consisting of geometrical differences between the reference Blade (Blade A) and the secondary blade (Blade B), as shown in Figure 3.

The two blades differed particularly in the tip shape. More specifically, Figure 4 highlights both an in-plane more advanced position and an out-of-plane lower position of the Blade B leading edge with respect to that of Blade A.

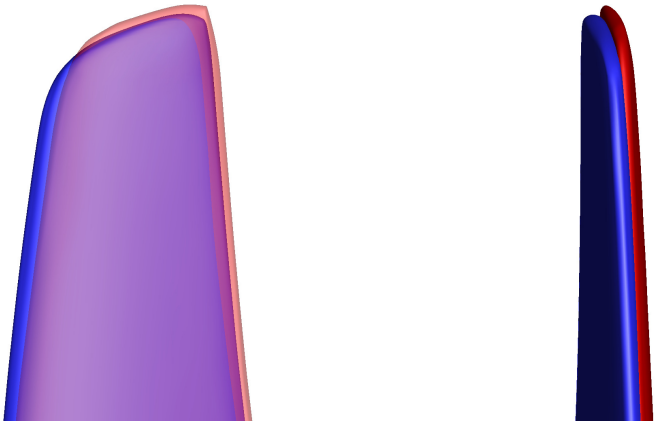

Figure 3. Geometry of Blade A (red) and Blade B (blue) overlapped.

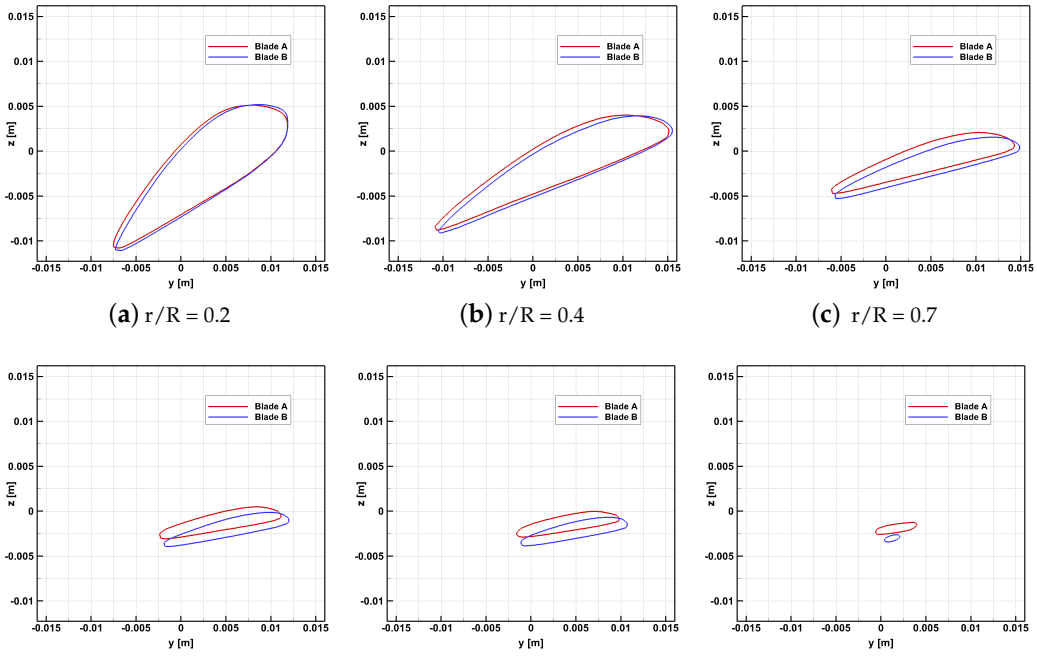

Figure 4. Comparison of Blade A and Blade B airfoil sections.

The investigated propeller was the object of a comprehensive experimental campaign performed in collaboration between DLR and CIRA with a combined experimental setup focused on aerodynamic interactional effects of co-axial propellers. The details are reported in the works by Yin et al. [6], De Gregorio et al. [2], and Rossignol et al. [7]. Results of the tests performed in this framework for a single propeller were considered to be a reference for the validation of the numerical methodology developed in the present work. Test results included both aerodynamic performance data acquired in terms of thrust and torque by a six-component load cell and flow field data obtained by PIV measurements. Moreover, acoustic data were obtained by a single pressure field microphone mounted on a 3-axis

traversing system. Readers are referred to [2,3,8] for details on the experimental setup and early results.

2.2. Numerical Methodology

The numerical investigation was performed using CIRA's in-house RAMSYS code [4], which is an unsteady, inviscid, and incompressible free-wake vortex lattice Boundary Element Method (BEM) solver for multirotor, multi-body configurations developed at CIRA. It is based on Morino's boundary integral formulation for the solution of the Laplace equation for the velocity potential φ [9]. The novel formulation proposed by Gennaretti et al. [10] was applied in RAMSYS to avoid the instabilities arising in the numerical formulation when wake panels are too close to or impinge the body. Readers are referred to [4] for details on the mathematical formulation of the code.

In rotary-wing aerodynamics, tip vortices play a major role in the quantification of the blade loads. Tip vortex models used in rotor wake simulations are typically specified in terms of a 2D tangential (swirl) velocity profile. The other velocity components (the axial and radial) are small and are usually neglected in most applications. This, however, may not be a justifiable assumption at young wake ages. The challenge is to properly reproduce the vortex behavior, but little is known about its core structure and dissipative/diffusive mechanisms [11]. Vatistas introduced an analytical model for the swirl velocity V_θ, as follows:

$$V_\theta = \frac{\Gamma_V}{2\pi} \frac{r}{(r_c^{2n} + r^{2n})^{1/n}}. \tag{1}$$

It is expressed as a function of radial distance from the vortex center and shows a direct proportionality with respect to vortex filament circulation Γ_V and vortex core radius r_c. A family of curves can be generated by tuning the exponent n. When n approaches $+\infty$, Vatistas approximates Rankine's swirl velocity. In this case, the vortex core is modeled as a rotating solid body, and the outer region $r > r_c$ follows the potential law [12]. It is important to observe the discontinuity produced at the vortex core radius. The exponent $n = 1$ represents the Kaufmann vortex [13], also known as the Scully model [14]. It exploits an algebraic formulation to solve the discontinuity observed in Rankine's formulation. Another possibility is to have $n = 2$. In this case, the Vatistas model is the approximation of the Lamb–Oseen model [15,16].

To account for the vortex core growth with time, the model formulated by Bhagwat–Leishman was implemented in RAMSYS [17], in which the diffusive growth of a viscous vortex is an extension of the classic Lamb–Oseen [16] core growth model with an average apparent or eddy viscosity correction δ for the effects of self-generated turbulence. The apparent viscosity parameter, as given by Squire's hypothesis [18], is estimated based on several sets of experimental results documenting the characteristics of trailing tip vortices [19]. In this model, the core radius growth r_c is equal to:

$$r_c(t) = \sqrt{4\alpha\delta\nu \frac{z + z_0}{V_\infty}} = \sqrt{r_0^2 + \frac{4\alpha\delta\nu\Psi}{\Omega}}. \tag{2}$$

The axial direction coordinate z_0 generally has a finite core radius size at the initial time instant t_0 and finite induced velocity. The velocity V_∞ is the velocity in the axial direction under the rotor, and it represents the convection velocity in the same direction. The formulation exploits the Oseen [15] parameter and the eddy viscosity coefficient δ. The latter one is proportional to the tip vortex circulation Γ_V as follows:

$$\delta = 1 + a_1 \frac{\Gamma_V}{\nu}. \tag{3}$$

The term Γ_V/ν is equal to the tip vortex Reynolds number Re_V, while a_1 is the Squire's empirical parameter specified to vary between 0.2 and 0.0002, as indicated in [17]. Finally, a time decay of the tip vortex circulation was considered. The exponential law suggested by Donaldson and Bilanin [20], proposed for fixed wing applications, define Γ_V as:

$$\Gamma_V(t) = \Gamma_0 exp(-\frac{bq}{S}t), \tag{4}$$

where b is a decay coefficient, q represents the ambient turbulence and S is a geometrical coefficient representing wing semi-span. For practical reasons, the term bq/S is expressed in this work as a single term b_1 called decay exponent.

A characteristic of the Bhagwat–Leishman model is represented by its flexibility. Indeed, being dependent on a set of user-defined parameters, it can be finely tuned to provide, in principle, an optimal match with the experimental data, regardless of the size of the rotor or propeller investigated and its operative tip Reynolds number. As previously highlighted, the goal of this work is the introduction of a procedure for the tuning of vortex and wake models to improve the prediction capabilities of mid-fidelity methods for the investigation of propellers. Therefore, the whole procedure depends on four parameters i.e., the n exponent in the Vatistas vortex core model; the initial core size r_0; the Squire coefficient a_1; and the decay exponent b_1, which are evaluated through an optimization procedure that will be described in Section 2.2.2.

2.2.1. Propeller Numerical Model

The geometry used in the numerical simulations does not consider the hub and models the blade from a root cut-out station set at r = 0.04 m. In order to replicate the experimental setup in the numerical investigations, the fairing of the rotor support (pylon) was also modeled (see Figure 5) as an aerodynamic surface made by Joukowsky's airfoil sections, ensuring no flow separation at the Reynolds numbers of the investigations [6]. The chord length of the pylon is constant and equal to c_{pylon} = 0.2 m along the first 51.26% of the height, then it is tapered up to a chord length equal to c_{pylon} = 0.151 m at the top. The propeller axis of rotation was located 0.04 m downstream of the fairing leading edge.

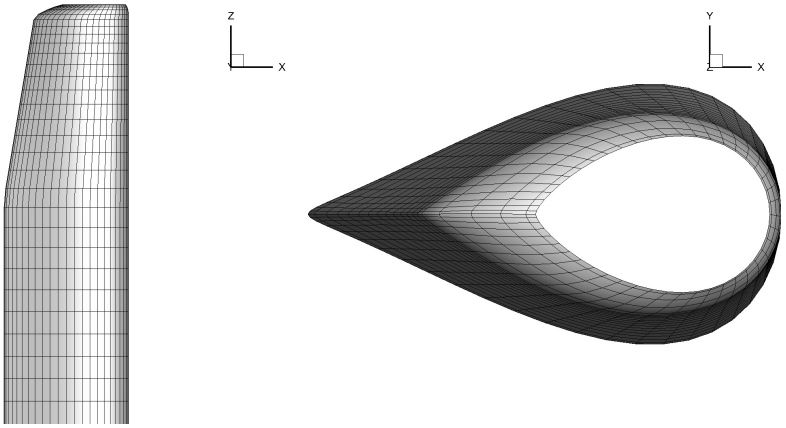

(**a**) Side View (**b**) Top View

Figure 5. Mesh of the Pylon Geometry.

The main issue regarding the propeller geometry was the difference between the two blades due to manufacturing inaccuracies. In order to build a consistent numerical setup, a suitable number of panels was applied along spanwise and chordwise directions to model accurately the different curvatures, especially approaching the tip region (see Figure 6). The surface mesh was not uniform. Indeed, a finer discretization was applied chordwise toward the leading edge and spanwise toward the blade tip.

The test condition selected for the numerical simulations is hover with a propeller angular velocity Ω equal to 10,120 rpm, which corresponds to a tip speed of $V_{tip} = 174.86\ \frac{m}{s}$. The vortex core model implemented in RAMSYS requires as input data: the Squire coefficient a_1, the Vatistas exponent n, the decay exponent b_1, and the initial vortex core radius non-dimensionalized with respect to chord length r_0/c. A baseline condition of the propeller was defined by selecting as initial values for the parameters the set reported in Table 1 usually applied by CIRA for small-scale helicopter rotors simulations. These parameters were used for the sensitivity studies described in the following.

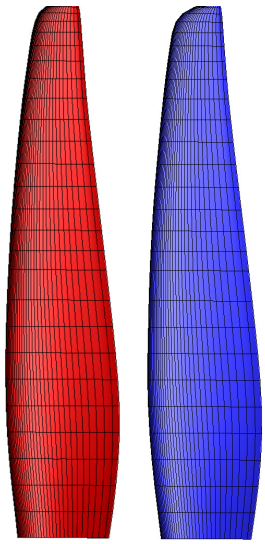

Figure 6. Mesh for Blade A (red) and Blade B (blue).

Table 1. Baseline Vortex and Wake Model Parameters used for RAMSYS simulations.

	a_1	b_1	n	r_0/c
Baseline	3×10^{-4}	2.5	1	0.05

A grid sensitivity analysis was performed on the full propeller to remove any dependence on the grid. Panel methods are particularly sensitive to the aspect ratio of each panel. This was kept roughly constant and equal to 2.1 in all the discretization generated for the sensitivity analysis, from the coarse to the fine one. The resulting number of panels for the three grids is summarized in Table 2. The average propeller thrust coefficient C_T computed on the last revolution for the three grids was compared to the experimental value $C_{T_{exp}}$ to evaluate the accuracy of the numerical model. In particular, the non-dimensional coefficient ΔC_T calculated as $\Delta C_T = \frac{C_T - C_{T_{exp}}}{C_{T_{exp}}} \times 100$ was reported in Table 2 showing that the fine grid produced a quite accurate agreement with the experimental value. Therefore, the fine mesh was used in all the following simulations and for the optimization process.

Another important parameter affecting the results was the number of revolutions of the propeller, which was also set equal to the number of wake spirals. A sensitivity analysis was performed by considering up to 11 propeller revolutions. The average propeller thrust coefficient C_T was computed for each of the last three revolutions as well as the error

computed as $err = \frac{C_{T_i} - C_{T_{i-1}}}{C_{T_{i-1}}} \times 100$, with i being the index of the revolution number. Results of this study reported in Table 3 show that ten revolutions can be chosen as a trade-off solution between the err value, sufficiently small, and the computational time effort.

Table 2. Parameters of grid sensitivity analysis.

	Chordwise Panels	Spanwise Panels	ΔC_T [%]
Coarse	42	17	−7.11
Medium	50	21	−3.07
Fine	60	26	−0.15

Table 3. Parameters of propeller revolutions analysis.

	C_T	err [%]
Rev. #9	0.09922	-
Rev. #10	0.09930	0.08
Rev. #11	0.09932	0.02

The time histories of the propeller thrust coefficient computed using the three grids defined in Table 2 for 10 propeller revolutions are shown in Figure 7. This representation confirmed the convergence of the solutions obtained with all the grids.

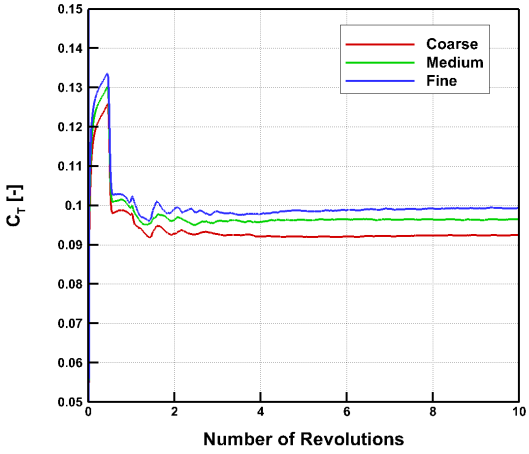

Figure 7. Time histories of the computed propeller thrust coefficient with different grid refinements.

The blade azimuth angle step selected for the evolution of the free-wake $\Delta\Psi_w$ was equal to 2° in all the following simulations. This term was related to the numerical scheme, and its value had to be a trade-off between truncation error and an increase in the computational time. Indeed, using a finite-difference explicit scheme to describe the evolution of the wake, an error proportional to $(\Delta\Psi_w)^2$ is introduced. Smaller steps were not considered due to the excessive computational time that would have been required.

2.2.2. Optimization Methodology

The goal of the optimization was to identify the most suitable combination of the wake model parameters, i.e., a_1, b_1, n and r_0/c defined earlier, providing a numerical solution resembling as close as possible experimental results. In particular, two different initial core radii for Blade A $(r_0/c)_1$ and Blade B $(r_0/c)_2$ were considered as they are characterized by some differences in the geometry. A fitness function was defined to quantify the error between the numerical and experimental solutions. In this specific case, the fitness

function was built considering the induced velocities evaluated in a vertical plane of the average flow field below the propeller disk. In particular, five crossflow profiles, i.e., at $z/R = -0.1, -0.2, -0.3, -0.4$, and -0.5, were selected to take into account the behavior of the wake downwash moving away from the propeller disk (see Figure 8(left)). Further downstream of $z/R = -0.5$, it becomes more difficult to properly account for the vortex characteristics at higher wake ages due to a tendency of the real flow to become non-periodic [21]. For each i-th plane, the differences between the numerical and experimental vertical component of the induced velocity w were first evaluated in N points along the radial direction $0.3 \leq x/R \leq 0.9$ (see Figure 8(right)). Therefore, the fitness function for the i-th plane was defined as:

$$f_{w_i} = \sqrt{\frac{\sum_j (w_{num}(x/R) - w_{exp}(x/R))^2}{N}}. \tag{5}$$

Finally, the global fitness function f_w was then computed as:

$$f_w = \sum_i f_{w_i}. \tag{6}$$

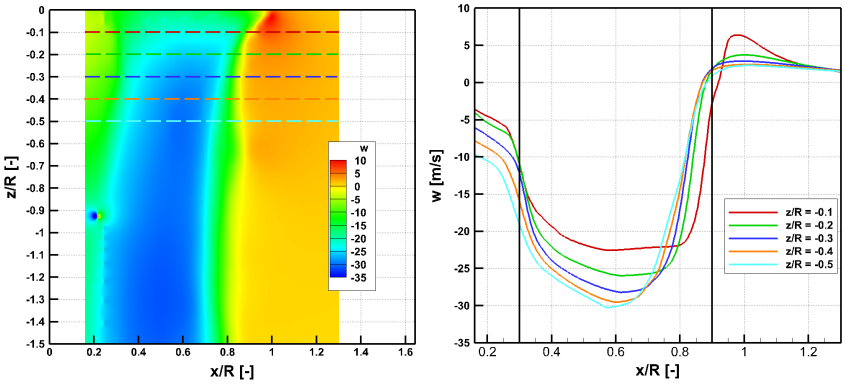

Figure 8. PIV flow field (**left**) and induced velocity profiles (**right**) considered to build the fitness function.

The properties of the identified fitness function required the use of approaches exhibiting a lower sensitivity to numerical instabilities that could occur, especially in hovering conditions, when modeling a large number of free-wake revolutions. For this reason the gradient-free methods, as the genetic algorithms, were preferred to gradient-based approaches.

The software used to solve the design optimization problem is the ADGLIB library (ADaptive Genetic algorithm LIBrary) [22]. It is an evolutionary optimization software library developed at CIRA based on the hybridization concept. ADGLIB allows the easy definition of evolutionary optimization algorithms that combine, for example, classical bit-string-based genetic algorithms (24-bit for each parameter) with hill-climbing specialized operators. The choice is motivated by the need to improve the efficiency of genetic algorithms while keeping their flexibility in searching large design spaces, thus enhancing their exploration capabilities. ADGLIB allows the definition of scalar and vectorial input/output variables and constants and is capable of performing both single and multi-objective optimization. The initial population distribution is obtained by the quasi-random low discrepancy Sobol's sequence [23].

2.3. Acoustic Simulations

Acoustic simulations were performed for a final evaluation of the improvements obtained in the aerodynamic calculations of the propeller, taking into account the differ-

ences between the geometries of the two blades and the selection of suitable vortex core parameters by the optimization procedure. The evaluation of the aeroacoustic free-field was performed by the ACO-FWH solver based on FW-H formulation [24,25] using as input the aerodynamic solution evaluated by RAMSYS and consisting of the rotor blade pressure distributions. The advanced-time formulation of Farassat 1A [26] was employed, and the linear terms (the so-called thickness and loading noise contributions) are computed through integrals both on the moving blades surface (impermeable/rigid surface formulation) and on the fixed surfaces. The quadrupole contribution due to the nonlinear terms distributed in the perturbed field around the blade is neglected. Considering that the propeller wake strongly interacts with the pylon, it contributes to noise generation.

In the numerical analysis of the acoustic field, 16 microphones were placed in the vicinity of the test rig and reproducing the experimental setup [3]. In particular, the microphones were installed in two linear arrays, Figure 9 left, and on a circular arc of radius 0.3 m with a spacing between the microphones of 15 deg, Figure 9 right.

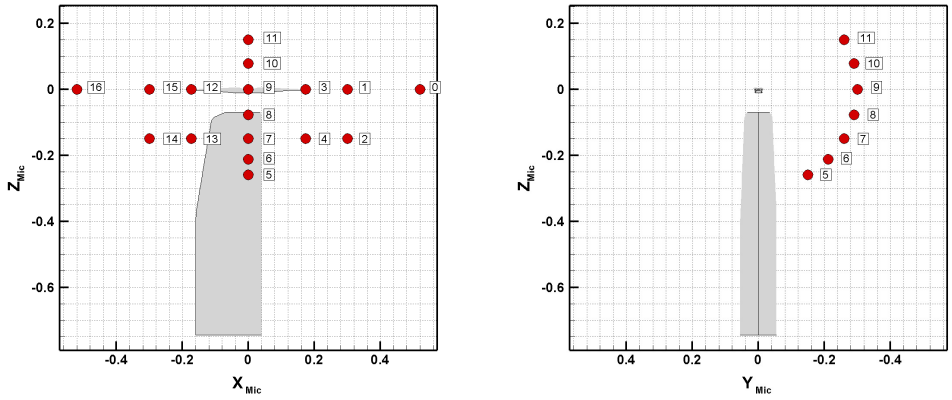

Figure 9. Microphones Setup for acoustic validation [3].

The acoustic results were represented in terms of spectra of the Sound Pressure Level (SPL). In order to compute them, an advanced-time formulation of the FW-H analogy was first used for computing the acoustic pressure in the time domain. The frequency-domain counterpart of the acoustic pressure was then achieved by applying the Fast Fourier Transform (FFT). According to this, the SPL is finally computed to represent the acoustic spectrum for each microphone, according to:

$$SPL(f) = 20log_{10}(\frac{P'_{rms}(f)}{P_{ref}}) \tag{7}$$

where the reference pressure P_{ref} is defined as $P_{ref} = 20$ µPa and $P'_{rms}(f)$ is defined as:

$$P'_{rms}(f) = |\hat{p}(f)|/\sqrt{(2)} \tag{8}$$

with $|\hat{p}|$ is the module of the acoustic pressure in the frequency domain achieved with the FFT.

3. Results and Discussion

3.1. Aerodynamic Results Analysis

In this section, aerodynamic simulation results obtained by the optimization procedure are reported and compared to the ones obtained with baseline parameters as well as with experiments. The design variables for the initial vortex core size of the two blades, i.e., $(r_0/c)_1$ for Blade A and $(r_0/c)_2$ for Blade B, started from the same value but different values

were explored since the first generation. The optimized core sizes were then obtained equal to 0.146 for $(r_0/c)_1$ and 0.199 for $(r_0/c)_2$. These results were found to be in good agreement with the equivalent experimental value obtained for Blade A, i.e., around $r_0/c = 0.15$. The decay coefficient b_1 trend toward optimal values showed only a mild change from baseline value, as it was found to be equal to 2.653, with an increase of 6.12%. On the other hand, the trend observed for Vatistas coefficient n led to an optimal value of 2.28, quite higher than the baseline value equal to 1. The numerical optimization pushed a_1 Squire's coefficient towards higher values, reaching 0.01265. This is two orders of magnitude higher than the baseline value, i.e., equal to 3×10^{-4}. These results demonstrate that the diffusion for the original model was not sufficient, and an additional level of turbulent diffusion was then required to improve accuracy. Finally, the behavior of the fitness function (6) was reported in Figure 10. The optimization procedure provided a value of the fitness function $f = 7.66$ with respect to the baseline value $f = 10.14$.

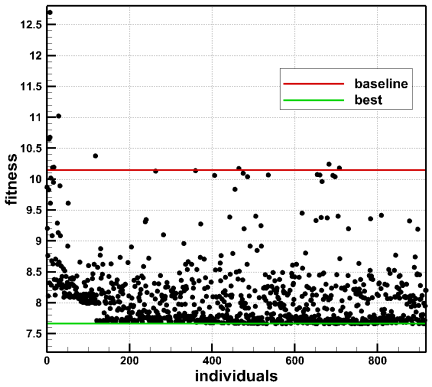

Figure 10. Fitness Function in the Optimization Development.

The optimized set of parameters (Best) is reported in Table 4 and compared with baseline one.

Table 4. Baseline and optimized Vortex and Wake Model Parameters.

	a_1	b_1	n	$(r_0/c)_1$	$(r_0/c)_2$	f
Baseline	3.000×10^{-4}	2.500	1.00	0.050	0.050	10.14
Best	1.265×10^{-2}	2.653	2.28	0.146	0.199	7.66

This new set of parameters was used to perform aerodynamic simulations to assess the improvements obtained by the application of the optimization procedure. Table 5 shows the comparison of the propeller thrust coefficients obtained from simulations performed with the baseline and best vortex and wake model parameters, as well as the differences with respect to the mean experimental value.

The thrust coefficient C_T obtained with best parameters differs with respect to baseline simulation value of about 0.6%, while discrepancy with the experimental is found to be $\Delta C_T = -0.72\%$. These small variations in the thrust coefficient are expected since the optimization procedure was conceived to improve the induced velocity behavior only.

Table 5. Thrust Coefficient comparison for Optimized investigation.

	C_T [−]	ΔC_T [%]
Exp	0.09945 ± 0.000992	-
Base	0.09930	−0.15
Best	0.09874	−0.72

Therefore, the tip vortex displacements are analyzed, both comparing geometrical characteristics of the wake vortical tube boundaries, highlighted by the tip vortex filament [27] and comparing vorticity properties using the Γ_2 method, a vortex detection criterion formulated by Graftieux et al. [28,29], to identify the vortices tracks. Figure 11 shows the comparison of the streamtubes obtained for two blades with the baseline and optimized simulations. Similarities of the two solutions up to 2–3 revolutions are apparent. In particular, the characteristics of the evolution of the baseline wake led the tip vortex filaments to diffuse rapidly, making not possible to preserve their structure. On the other hand, for the optimized simulation, the tip vortex filaments are preserved up to 10 revolutions, providing, at the same time, a clear view of the contraction and development of the streamtube.

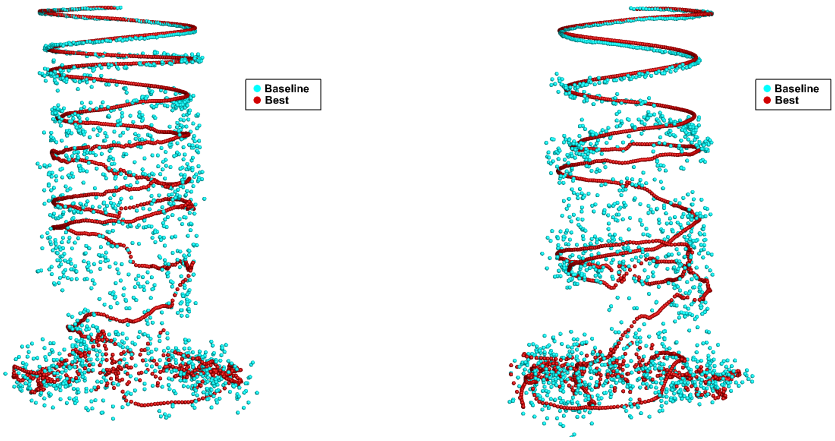

(**a**) Blade A (**b**) Blade B

Figure 11. Tip Vortex Filament comparison for Optimized investigation.

The vortex tracks collected at several blade azimuthal phase angles Ψ_b and identified using the Γ_2 method are compared in Figure 12.

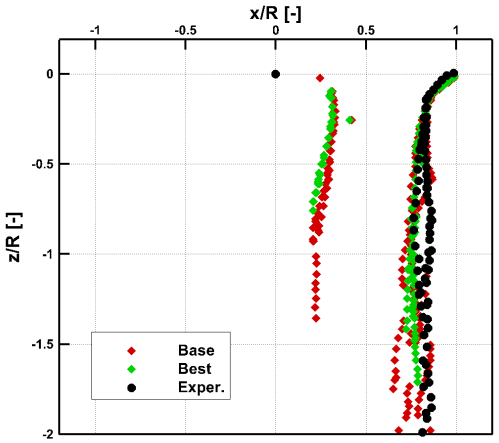

Figure 12. Vortex Track comparison for Optimized Investigation obtained by superimposing several phase-locked results.

The numerical trend properly approximates the experimental one for both the baseline and optimized simulations, and only slight differences can be observed. In particular, for $z/R \leq -0.5$, the baseline model does not show a good correlation with experimental results as the path of the external vortices is not visible. Furthermore, the internal path is better re-traced by the optimized set of parameters, particularly for z/R between -0.5 and -1, whereas, for $z/R \leq -0.5$, it is not possible to identify the external path. Thus, in order

to provide a clearer comparison, Figure 13 shows the comparison of the tip vortices paths obtained at two separate blade azimuthal phase angles, i.e., $\Psi_b = 0°$ and $\Psi_b = 30°$.

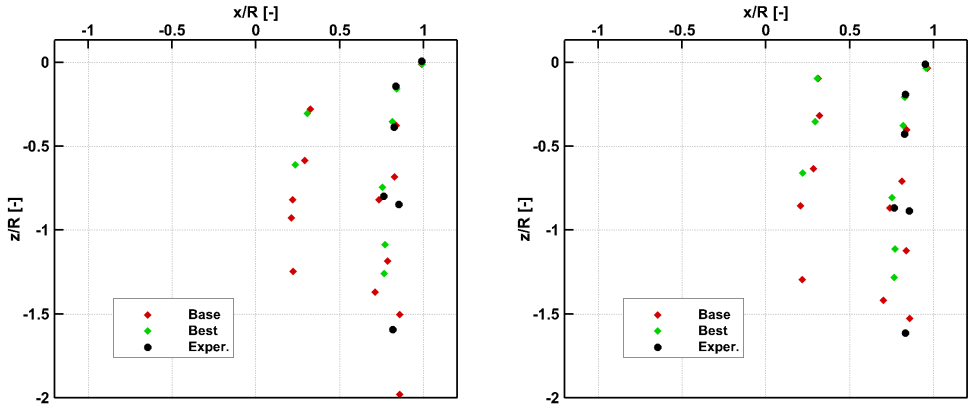

(**a**) $\Psi_b = 0°$ (**b**) $\Psi_b = 30°$

Figure 13. Vortex Track comparison obtained for two separate blade azimuthal angles.

For $\Psi_b = 0°$, a couple of vortices were detected in the region included in $0.8 \leq x/R \leq 1$ and $-1 \leq z/R \leq -0.5$ showing different characteristics both for the baseline and experimental analysis (see Figure 13a). This was not present in the numerical optimized investigation. Moreover, the same observation can be verified at different blade azimuth angles as $\Psi_b = 30°$ (see Figure 13b). In order to explain this behavior, the tip vortex filaments superimposed to the numerical flow field represented by means of vorticity magnitude contours are shown in Figure 14 for the optimized solution obtained at $\Psi_b = 0°$ and $\Psi_b = 30°$.

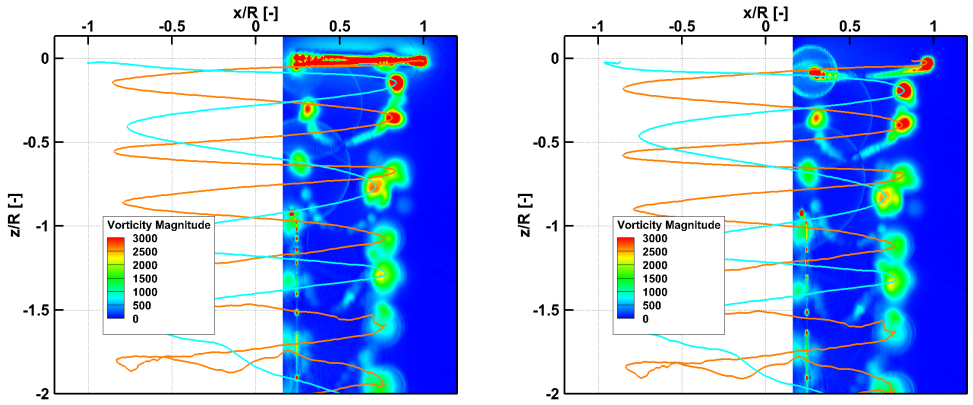

(**a**) $\Psi_b = 0°$ (**b**) $\Psi_b = 30°$

Figure 14. Tip Vortex Filament superimposed to the vorticity magnitude field for Optimized Investigation obtained for two separate blade azimuthal angles.

In the above-mentioned region, the filaments reproduce the couple described, but the equivalent vorticity is not able to reproduce the phenomenon properly. Indeed, increasing the value of Squire's coefficient, the turbulent diffusion increased, and the vorticity of the two vortices merged, thus not allowing the identification of two separate vortices by Graftieux's method.

To better understand the advantages introduced by the optimization procedure, the axial velocity profiles obtained from the average flow field downstream of the propeller disk were compared at different values of z/R in Figure 15.

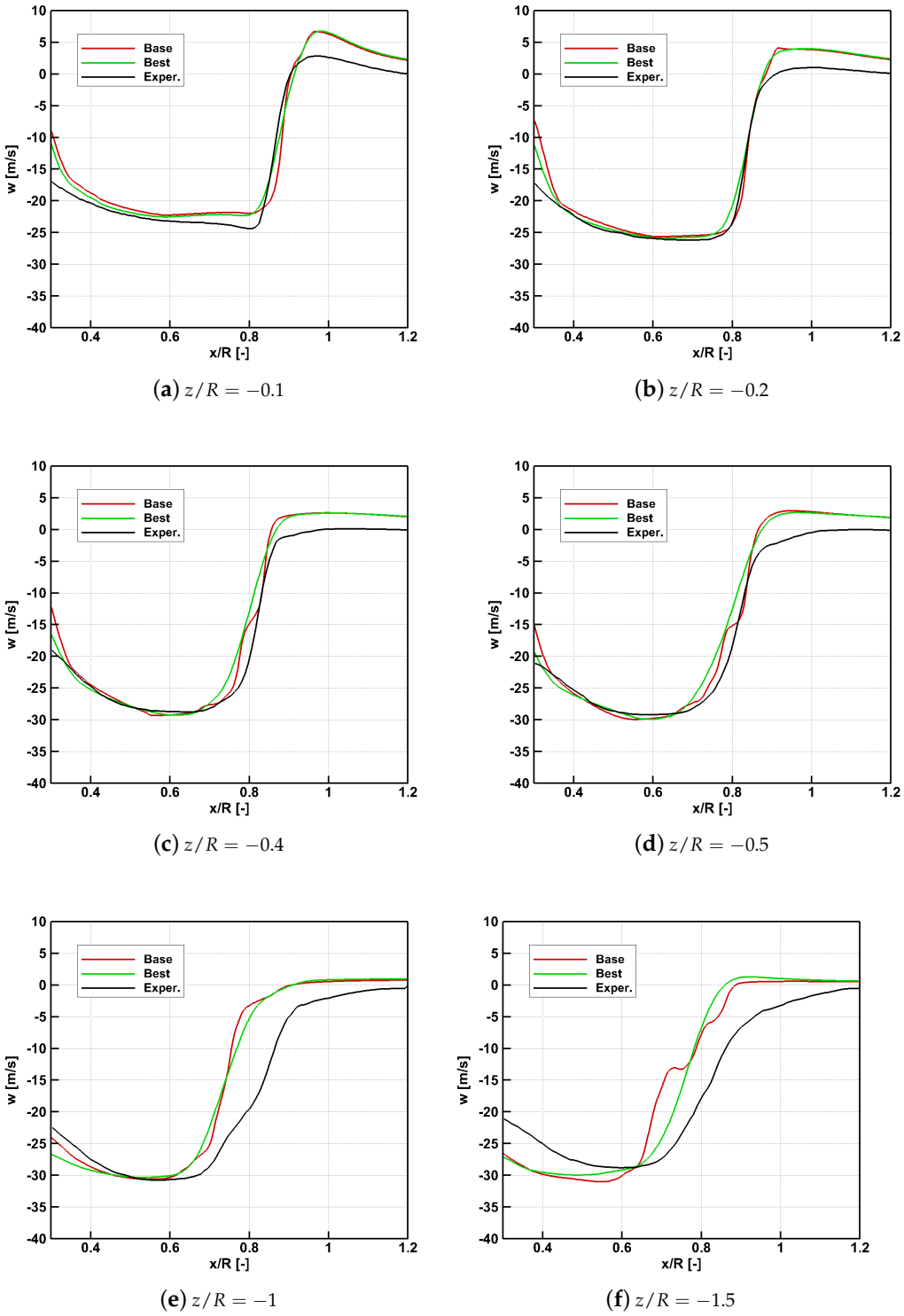

(**a**) $z/R = -0.1$ (**b**) $z/R = -0.2$

(**c**) $z/R = -0.4$ (**d**) $z/R = -0.5$

(**e**) $z/R = -1$ (**f**) $z/R = -1.5$

Figure 15. Induced Axial Velocity comparison on several horizontal profiles downstream propeller disk.

The axial velocity comparisons show a general global improvement obtained by optimized simulation with respect to experiments. In particular, at $z/R = -0.1$, a slight improvement can be observed on the minimum value before approaching the shear layer (see Figure 15a). Neither the baseline nor the numerical optimization are able to exactly reproduce the experimental slope within the shear layer region since the former overestimates it, while the latter underestimates it. On the other hand, at $z/R = -0.2$, the baseline numerical investigation can better reproduce the behavior of the curve in the shear

layer region between $0.8 \leq x/R \leq 0.9$ (see Figure 15b). The numerical optimization is not equally accurate, although, in the second half of the shear layer region, it shows a good correlation with the experimental results. In addition, for lower values of x/R, the optimized case improves the baseline solution, approximating with higher accuracy the experimental behavior from $x/R = 0.4$.

For $z/R = -0.4$ and $z/R = -0.5$, no major differences for $x/R \leq 0.7$ can be appreciated as both simulations were able to reproduce with enough fidelity the experimental curve (see Figure 15c,d). Nevertheless, the baseline one shows a non-monotonic behavior in the shear layer region. In this region, the curve presents two different slopes, both far from the experimental one. On the other hand, the optimized case curves keep a smooth trend within the whole region, improving the numerical slope at the same time.

The advantages brought by the optimization procedure are more evident by comparing axial velocity profiles at $z/R = -1$ and $x/R = -1.5$ (see Figure 15e,f), as adjusting the diffusive and dissipative characteristics led to a shear layer with improved correlation to the experimental case. To better show this behavior, the first derivative of the axial velocity calculated with respect to the radial direction is compared in Figure 16 over four profiles at different z/R.

Outside the shear layer region, the numerical simulation approaches the experimental behavior with good accuracy. For slices $z/R = -0.1$ and $z/R = -0.2$, the trend in the shear layer is reproduced correctly by both simulations (see Figure 16a,b). Nevertheless, the baseline one produces a secondary peak at $x/R = 0.9$, which is not present in the experimental results. In addition, the peak is overestimated for the baseline case and underestimated for the optimized case, but generally, the optimized simulation produces more accurate results.

For slices at $z/R = -1$ and $z/R = -1.5$ (see Figure 16c,d), these advantages are more evident as the baseline is not able to follow the experimental behavior. On the other hand, the optimized numerical simulation provided a satisfying correlation to experimental results but with a translation of the shear layer toward the inner region. Nevertheless, the peak value, the shear layer width, and the axial velocity slope in this region are correctly reproduced.

Up to this stage, only the global characteristics of the flow field were considered to be the optimization procedure set to improve the averaged flow field. Considerations on the local properties of the tip vortices were then provided by comparing the tangential velocity V_θ and circulation Γ_v of single tip vortices. Graftieux's Γ_2 method computes the vortex properties in the radial direction and evaluates at $r = 0$ the center of the identified viscous core. More specifically, the swirl velocity, the circulation, the radial velocity, and the vorticity were computed, and the first two were used to compare the numerical simulations to experimental results as they were directly influenced by the optimization parameters.

The experimental results at $\Psi_b = 30^\circ$ were considered to be a benchmark for this quantitative comparison of vortex characteristics. Only the first two vortices below the propeller disk were considered, i.e., Vortex 1 and Vortex 2. Figure 17 shows the comparison of the V_θ velocity calculated for the two vortices under investigation at $\Psi_b = 30^\circ$. It is clear that for both vortices, the baseline results overestimate the maximum value of the swirl velocity and underestimate the vortex core radius. On the other hand, the optimized simulation provides a better correlation with the experimental result for Vortex 1. For Vortex 2, the numerical optimized results overestimate the core radius and underestimate the swirl velocity V_θ.

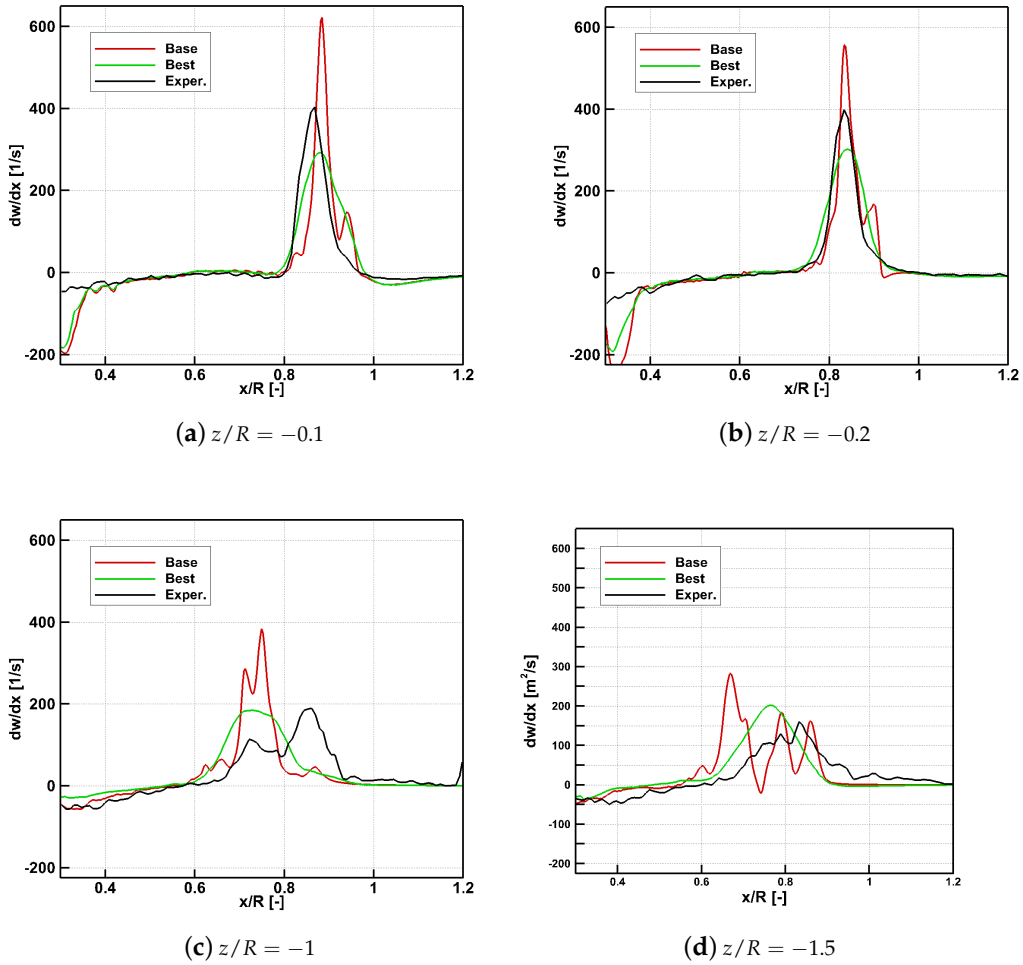

(**a**) $z/R = -0.1$ (**b**) $z/R = -0.2$

(**c**) $z/R = -1$ (**d**) $z/R = -1.5$

Figure 16. Induced Axial Velocity Derivative comparison on several horizontal profiles downstream propeller disk.

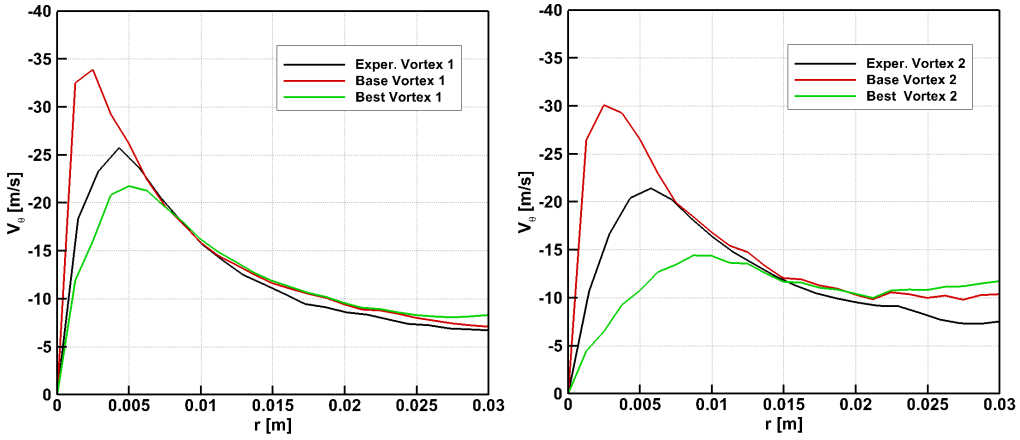

(**a**) Vortex 1 (**b**) Vortex 2

Figure 17. Tip Vortex Swirl Velocity comparison at $\Psi_b = 30°$.

The tip vortex circulation Γ_V comparison is reported in Figure 18. It is possible to observe that for Vortex 1, the numerical simulation shows a good agreement with experiments in terms of circulation (see Figure 18a). On the other hand, for Vortex 2, higher discrepancies with respect to experiments are also found for the optimized simulation (see Figure 18b).

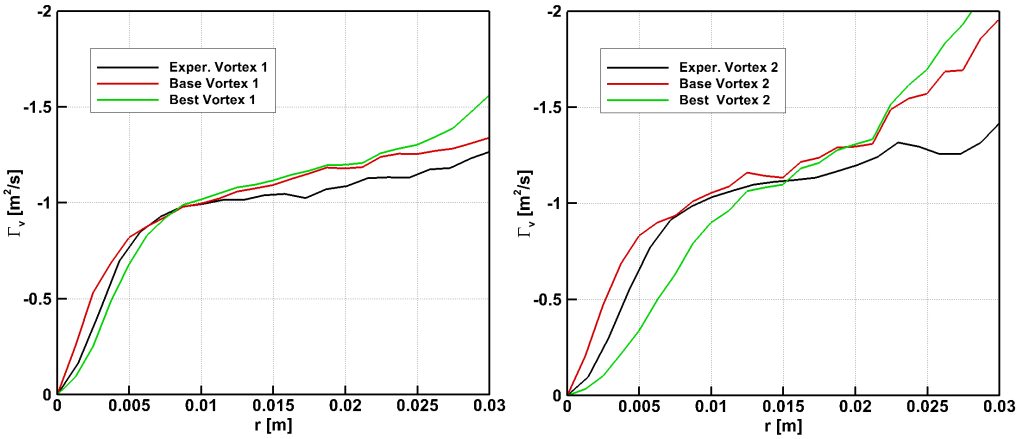

(**a**) Vortex 1 (**b**) Vortex 2

Figure 18. Tip Vortex Circulation comparison at $\Psi_b = 30°$.

This effect is mainly proven by the fact that Vortex 2 was captured with the wake age $\Psi = 210°$ where the diffusive and dissipative properties of the wake model grew in an order of magnitudes. In particular, the vortex core radius is influenced by r_0/c and δ parameters. The latter one is described in Equation (3) and is itself influenced by a_1 and Γ_v, and then by the decay coefficient b_1. On the one hand, b_1 was not able to change the order of magnitude for δ as the differences in the circulation were not so strong, especially at $\Psi_b = 30°$. In addition, the optimization increased a_1 to values two orders of magnitudes higher than the baseline value. Therefore, in order to further improve the model capabilities, a second optimization procedure was performed, in which $(r_0/c)_1$, $(r_0/c)_2$, and n were kept equal to those obtained in the first optimization and limiting a_1 exponent to -3, thus keeping this latter parameter similar to the range defined by Leishman [30]. The results of this second optimization procedure produced no change in the value of the decay coefficient with respect to the first optimization. Thus, a second set of parameters was defined as Best 2, where only the value of a_1 was changed to 2.947×10^{-3} with respect to the Best 1 parameters values reported in Table 1. The comparison of the results obtained in terms of swirl velocity and circulation distributions between Best 1 and Best 2 solutions are reported in Figures 19 and 20.

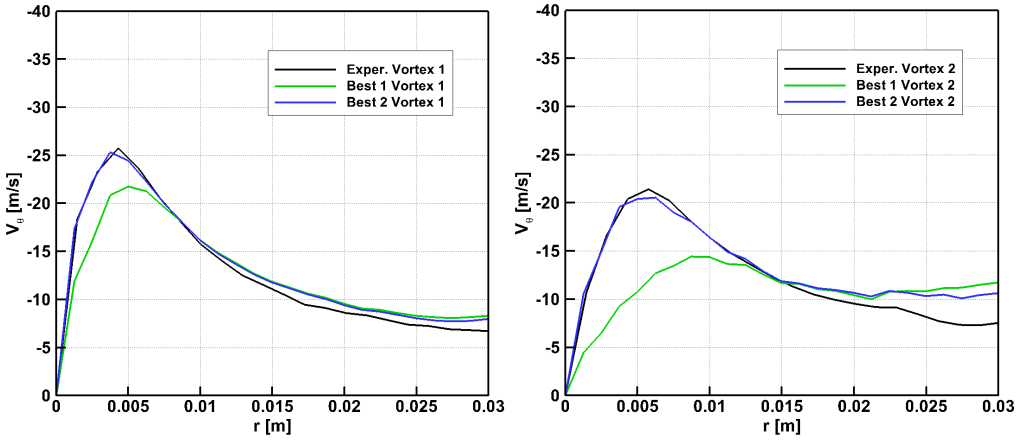

(**a**) Vortex 1 (**b**) Vortex 2

Figure 19. Tip Vortex Swirl Velocity comparison for Best 1 and Best 2 solutions at $\Psi_b = 30°$.

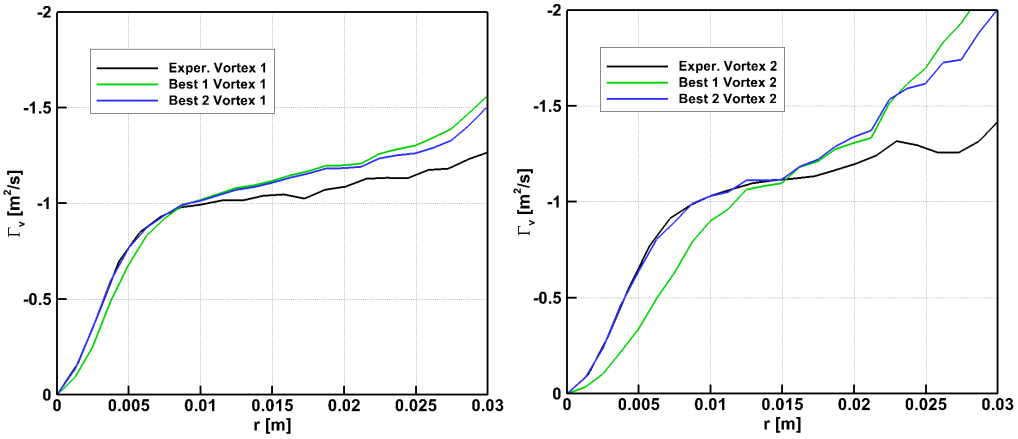

(**a**) Vortex 1 (**b**) Vortex 2

Figure 20. Tip Vortex Circulation comparison for Best 1 and Best 2 solutions at $\Psi_b = 30°$.

The simulation based on the Best 2 parameters shows a considerable improvement in the accuracy for both the circulation and swirl velocity distributions. In particular, the circulation for Vortex 2 was quite similar to experimental behavior, even increasing the wake age (see Figure 20b).

Tables 6 and 7 summarize the comparison between the two vortices' characteristics, particularly highlighting the variations *Delta* with respect to experimental values obtained by simulations in terms of vortex core radius r_c and absolute peak of tangential velocity $|V_\theta|_{max}$.

Table 6. Comparison of Vortex 1 radius r_c and absolute peak of tangential velocity $|V_\theta|_{max}$.

	r_c/c [−]	$\Delta r_c/c$ [%]	$\|V_\theta\|_{max}$ [m/s]	$\Delta\|V_\theta\|_{max}$ [%]
Exp	0.231	-	25.75	-
Base	0.129	−44.16	33.84	+31.42
Best	0.265	+14.72	21.72	−15.65
Best 2	0.203	−12.12	25.3	−1.75

Table 7. Comparison of Vortex 2 radius r_c and absolute peak of tangential velocity $|V_\theta|_{max}$.

	r_c/c [−]	$\Delta r_c/c$ [%]	$\|V_\theta\|_{max}$ [m/s]	$\Delta\|V_\theta\|_{max}$ [%]
Exp	0.305	-	21.39	-
Base	0.135	−55.74	30.07	+40.58
Best	0.486	+59.34	14.4	−32.68
Best 2	0.327	+2.29	20.55	−3.93

Results comparison shows how the Best 2 solution can improve the evaluation of both vortices' characteristics, leading to consistently reducing the discrepancies with respect to experiments in terms of radius and swirl component peak. In Table 8, the thrust coefficient C_T for the BEST 2 simulation was reported and compared with the previous analysis. Negligible differences in aerodynamic performance are obtained.

Table 8. Thrust coefficient comparison.

	C_T [−]	ΔC_T [%]
Exp	0.09945 ± 0.000992	-
Base	0.09930	−0.15
Best 1	0.09874	−0.72
Best 2	0.09919	−0.26

Moreover, in Figure 21, the values of δ for the Baseline, Best 1 and Best 2 are reported and compared to the experimental value and literature references [19]. The Reynolds number for the tip vortex was equal to $Re_V = 2.39 \times 10^4$ then, recalling Equation (3), it was possible to compute the effective turbulent diffusion. The Baseline simulation produced a $\delta = 8.17$, Best 1 was two orders of magnitudes higher ($\delta = 303.26$). The experimental and Best 2 showed no significant discrepancies. Indeed, δ was equal to 66 for the former investigation and 71.4 for the latter one. Neither the baseline nor the first optimization were able to reproduce the experimental equivalent effective turbulent diffusion. Once again, focusing on the instantaneous properties of the vortex and limiting the growth for Squire's coefficient a_1 led to an improvement in the numerical-experimental correlation.

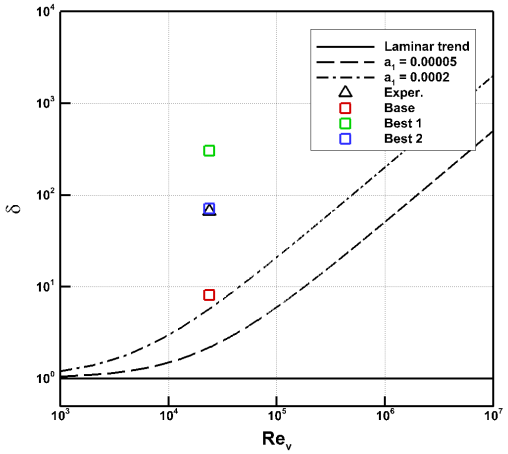

Figure 21. Effective Diffusion Constant δ comparison.

3.2. Acoustic Results Analysis

To also evaluate the effects of the optimization activity on the acoustic properties of the propeller, an aeroacoustic analysis was carried out using the aerodynamic solutions, namely the surface pressure distributions, obtained from the numerical simulations performed with:

1. Baseline vortex model parameters with propeller equipped with two equal Blades A (**BEB**);
2. Baseline vortex model parameters with propeller equipped with Blade A and Blade B (**BDB**);
3. Best 1 vortex model parameters with propeller equipped with Blade A and Blade B (**BST1**);
4. Best 2 vortex model parameters with propeller equipped with Blade A and Blade B (**BST2**).

Figure 22 shows the comparison with experiments [3] of the aeroacoustic spectra in terms of the SPL referring to microphones 02, 04, 07, 08, 13, and 14 as defined in Figure 9. In particular, the experimental results, published in [3], highlighted the presence of harmonics at every $(2k-1)$BPF/2, now on defined as sub-harmonics, where k is an integer in the

range $[1, +\infty]$ and BPF is the Blade Passage Frequency, i.e., equal to 337.33 Hz, defined as $N_B\Omega_{RPM}/60$, where N_B is the number of blades. Their presence was attributed to a noise component given by the electric motor but mainly by the dissimilarities of the two blades.

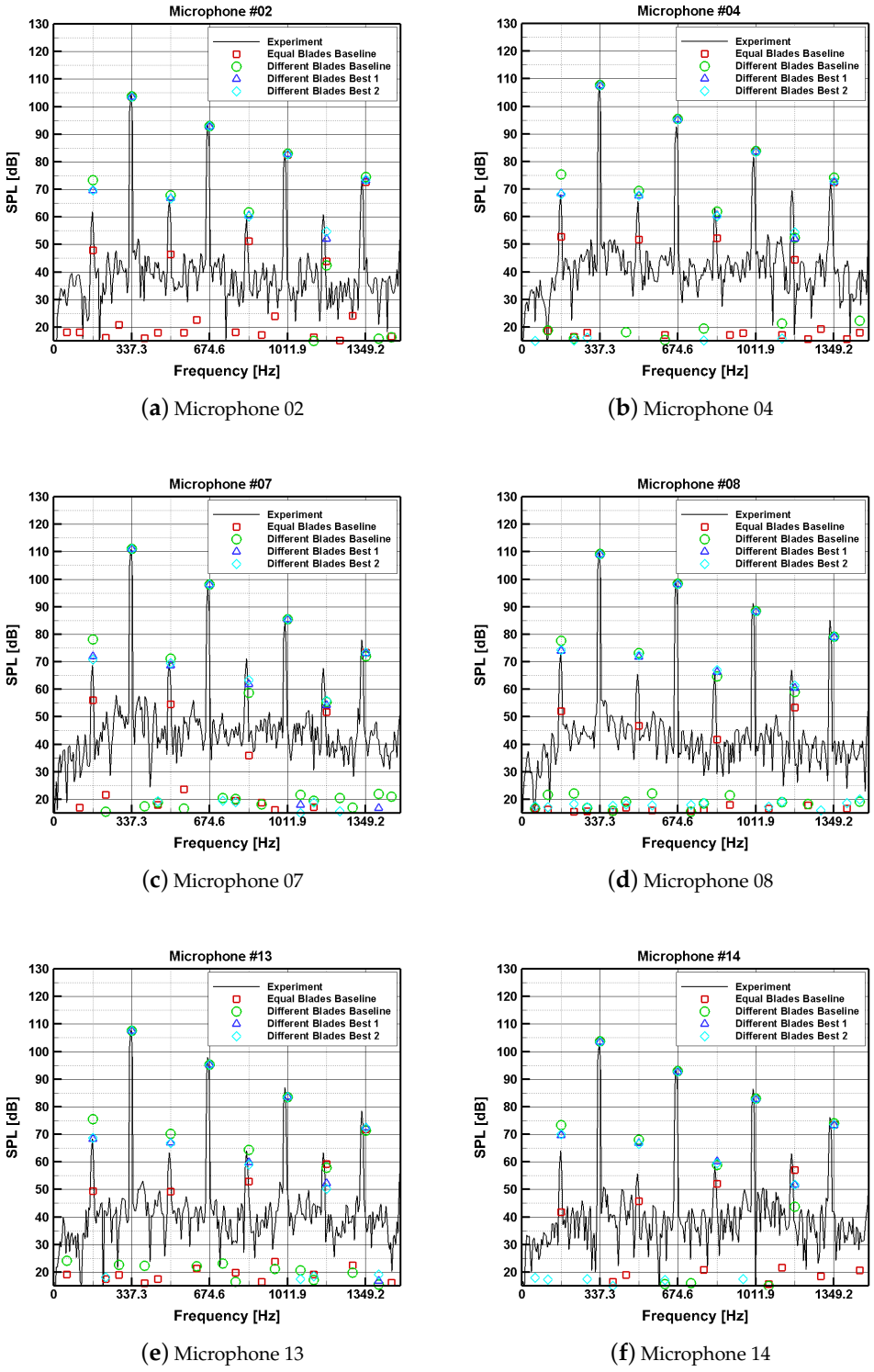

(**a**) Microphone 02 (**b**) Microphone 04

(**c**) Microphone 07 (**d**) Microphone 08

(**e**) Microphone 13 (**f**) Microphone 14

Figure 22. Comparison of SPL spectrum for different microphones.

Indeed, the **BEB** solution produced a significant underestimation of the sub-harmonics observed for all the investigated microphones, i.e., about 20 dB lower than the experiment in the first two BPF. This result was found to be common to all the medium-fidelity solvers solutions reported in [3], whereas an accurate estimation was only obtained by high-

fidelity Navier–Stokes CFD simulations. This outcome can be explained by the geometrical differences between the two blades, particularly in the tip region, thus producing tip vortices with different intensities and trailing from slightly different positions. These differences influence the flow field around the propeller, altering the interactional effects between the vortices inside the wake system and producing a non-negligible effect on the aeroacoustic signature of the propeller. In addition, it must be further stressed that in the medium-fidelity solver, the dissipative and diffusive properties of the flow are accounted for through a vortex core model, depending on a set of parameters, whose fine tuning can produce changes in the vortical properties of the wake, which, again, affects the aeroacoustics. Therefore, the disregard of the blade differences and the use of non-appropriate vortex core parameters can lead to inaccurate results. The use of a propeller with different blades, as in the **BDB** simulation, led to a huge improvement in the results, which are now in good agreement with the experiment. This confirms that the inaccuracy obtained by the **BEB** simulation was not a limit of the medium-fidelity methodology but is related to the incorrect blade geometrical modeling.

Further improvements to the accuracy of the sub-harmonics evaluation were obtained by the applications of the two optimization procedures, **BST1** and **BST2**, as it can be clearly observed from the comparisons over all the investigated microphones. Indeed, the **BDB** solution generally overestimates the SPL of the first sub-harmonic by 8 dB for mic 07 (see Figure 22c) and more than 5 dB for mic 04 and 13 (see Figure 22b,e). Instead, only negligible differences with respect to experiments can be observed for both **BST1** and **BST2** acoustic solutions. Finally, these improvements did not influence the prediction of the SPL at the BPF, as they are more influenced by the overall propeller loading. On the other hand, even if the effects on sub-harmonics could be considered less important with respect to BPFs for the evaluation of the global SPL, the obtained improvement of the methodology must be considered valuable due to the different implications of sub-harmonics on psychoacoustic knowledge and harmonic theory [31,32].

4. Conclusions

The present work was focused on the improvement of a free-wake model for the aerodynamic and aeroacoustic analysis of a small-scale two-bladed propeller in hover. The first goal of the work was to investigate the effects on aerodynamic and acoustic computations provided by geometrical discrepancies found between the two blades of the propeller caused by manufacturing inaccuracies. In particular, the proper geometrical modeling of the blades enabled the correct identification of the sub-harmonics of the SPL spectra, demonstrating that the initial inability found in the frame of the GARTEUR AG26 project was not produced by limits in the simulation capability of the medium-fidelity solver.

A second goal consisted of improving the Bhagwat–Leishman vortex core model used in RAMSYS to accurately predict rotor wake development. The approach followed in the work was based on two consecutive sets of an optimization procedure. The first one was aimed at identifying the most sui combination of the whole parameters able to reproduce as accurately as possible the global behavior of the experimental time-average induced velocity distribution below the propeller disk. In addition, the initial core radius was found to be different for the two blades as the solution is sensitive to the geometrical differences and subsequent vortex production characteristics. The second one was performed to understand the effects of Squire's turbulent diffusion coefficient a_1 and the decay coefficient b_1 on local characteristics of the tip vortex as the swirl velocity and related circulation. The optimization procedure exploited the evolutionary Genetic Algorithm for the selection of these parameters in their physical ranges by adjusting their value to match the diffusive

and dissipative properties of the experimental data. The combined effect of the two sets of optimizations further enhanced the improvements obtained in the evaluation of the experimental sub-harmonics in the SPL spectra obtained by modeling the blade dissimilarities. The results demonstrated the promising capabilities of a fine-tuned medium-fidelity approach to simulate the aerodynamic and acoustic details of a small-scale propeller in hover in the investigated setup, provided that the accurate geometrical modeling of the propeller and the selection of suitable parameters are carried out correctly. Based on the promising results obtained by this study, a more generalized procedure is planned to be validated against test cases characterized by different rotational speeds of a single propeller in hover and particularly for multi-propeller configurations.

Author Contributions: Conceptualization, A.V., D.Q. and F.D.G.; methodology, A.V., D.Q., F.D.G. and M.B.; software, A.V., D.Q., F.D.G. and M.B.; validation, M.I., A.V. and M.B.; formal analysis, A.V., D.Q., F.D.G. and M.B.; investigation, M.I., A.Z., A.V., F.D.G. and M.B.; resources, A.V., D.Q., F.D.G. and M.B.; data curation, A.V., F.D.G. and M.B.; writing—original draft preparation, M.I. and A.Z.; writing—review and editing, A.Z., A.V., D.Q., F.D.G. and M.B.; visualization, M.I., A.V., D.Q., F.D.G. and M.B.; supervision, A.Z., A.V. and D.Q. All authors have read and agreed to the published version of the manuscript.

Funding: This research received no external funding.

Data Availability Statement: Data could be available on request to authors.

Acknowledgments: The research leading to the presented results has been addressed within the framework of the RC/AG-26 "Noise Radiation and Propagation for Multirotor System Configurations", supported by GARTEUR.

Conflicts of Interest: The authors declare no conflicts of interest.

Abbreviations

The following abbreviations are used in this manuscript:

R	propeller radius	m
c	blade chord	m
σ	propeller solidity	m
C_T	thrust coefficient	-
C_Q	torque coefficient	-
Ω	Propeller speed	rad/s
Ω_{RPM}	Propeller speed	RPM
Γ_V	tip vortex circulation	m^2/s
Γ_0	initial vortex circulation	m^2/s
ν	kinematic viscosity	m^2/s
Re_V	tip vortex Reynolds number	-
r_c	vortex core radius	m
r_0	initial vortex core radius	m
α	Lamb–Oseen coefficient	-
n	Vatistas coefficient	-
b_1	decay exponent	-
a_1	Squire's coefficient	-
δ	effective diffusion constant	Pa
t	time	s
ϕ	velocity potential	m^2/s
V_∞	free-stream velocity	m/s
V_{tip}	blade tip velocity	m/s
V_θ	swirl velocity	m/s
w	axial velocity	m/s

f_{w_i}	i-th plane fitness function	-
f_w	global fitness function	-
Ψ	wake age	rad
Ψ_b	blade wake age	rad
$\Delta\Psi_w$	blade azimuthal revolution	rad
P_{ref}	reference pressure	Pa
P'	pressure fluctuations	Pa
P'_{rms}	root mean square of the pressure fluctuations	Pa

References

1. EASA. *Study on the Societal Acceptance of Urban Air Mobility in Europe*; Technical Report; EASA: Cologne, Germany, 2020.
2. De Gregorio, F.; Rossignol, K.S.; Ceglia, G.; Yin, J. Multi-rotor Wake Interaction Characterization. In Proceedings of the 49th European Rotorcraft Forum, Bückeburg, Germany, 5–7 September 2023.
3. Yin, J.; De Gregorio, F.; Rossignol, K.S.; Rottmann, L.; Ceglia, G.; Reboul, G.; Barakos, G.; Qiao, G.; Muth, M.; Kessler, M.; et al. Acoustic and Aerodynamic Evaluation of DLR Small-Scale Rotor Configurations within GARTEUR AG26. In Proceedings of the 49th European Rotorcraft Forum, Bückeburg, Germany, 5–7 September 2023.
4. Visingardi, A.; D'Alascio, A.; Pagano, A.; Renzoni, P. Validation of CIRA's Rotorcraft Aerodynamic Modelling System with DNW Experimental Data. In Proceedings of the 22nd European Rotorcraft Forum, Brighton, UK, 16–19 September 1996.
5. Xoar. PN Wooden Propeller. Available online: https://www.xoarintl.com/rc-propellers/electric-props/PJN-Electric-Beechwood-Propeller/ (accessed on 1 November 2024) .
6. Yin, J.; Rossignol, K.S.; Rottmann, L.; Schwarz, T. Numerical studies on small rotor configurations with validation using acoustic wind tunnel data. *CEAS Aeronaut. J.* **2024** , *15*, 671–702 . [CrossRef]
7. Rossignol, K.S.; Yin, J.; De Gregorio, F.; Visingardi, A.; Ceglia, G.; Barbarino, M.; Petrosino, F. Aeroacoustics of Small Contra-Rotating Co-Axial Rotors in Hover and Forward Flight. In Proceedings of the 2024 30th AIAA/CEAS Aeroacoustics Conference, Rome, Italy, 4–7 June 2024.
8. Rossignol, K.S.; Yin, J.; Rottmann, L. Investigation of Small-Scale Rotor Aeroacoustic in DLR's Acoustic Wind Tunnel Braunschweig. In Proceedings of the 28th AIAA/CEAS Aeroacoustics 2022 Conference , Southampton, UK, 14–17 June 2022. [CrossRef]
9. Morino, L. *A General Theory of Unsteady Compressible Potential Aerodynamics*; NASA Contractor Report; National Aeronautics and Space Administration: Washington, DC, USA, 1974.
10. Gennaretti, M.; Bernardini, G. Novel Boundary Integral Formulation for Blade-Vortex Interaction Aerodynamics of Helicopter Rotors. *AIAA J.* **2007**, *45*, 1169–1176. [CrossRef]
11. Widnall, S.E. The Structure and Dynamics of Vortex Filaments. *Annu. Rev. Fluid Mech.* **1975**, *7*, 141–165. [CrossRef]
12. Rankine, W.J.M. *Manual of Applied Mechanics*; C. Griffen Co.: London, UK, 1858.
13. Kaufmann, W. Über die Ausbreitung kreiszylindrischer Wirbel in zähen (viskosen) Flüssigkeiten. *Ingenieur-Archiv* **1962**, *31*, 1–9 . [CrossRef]
14. Lambert, P. *Helicopter Rotor Wake Geometry and Airloads and Helicopter Rotor Wakes*; Technical Report; Massachusetts Institute of Technology Cambridge Aerophysics Laboratory: Cambridge, MA, USA, 1972.
15. Oseen, C. *Über Wirbelbewegung in Einer Reibenden Flüssigkeit*; Arkiv för Matematik, Astronomi och Fysik; Almqvist & Wiksell: Stockholm, Sweden, 1912; Volume 4, pp. 14–21.
16. Lamb, H. *Hydrodynamics*, 6th ed.; Cambridge University Press: Cambridge, UK, 1932.
17. Bhagwat, M.; Leishman, J.G. Generalized viscous vortex model for application to free-vortex wake and aeroacoustic calculations. In Proceedings of the 58th Annual Forum and Technology Display of the American Helicopter Society International, Montreal, QC, Canada, 11–13 June 2002.
18. Squire, H.B. The Growth of a Vortex in Turbulent Flow. *Aeronaut. Q.* **1965**, *16*, 302–306. [CrossRef]
19. Ramasamy, M.; Leishman, J.G. The Interdependence of Straining and Viscous Diffusion Effects on Vorticity in Rotor Flow Fields. In Proceedings of the 59th Annual Forum and Technology Display of the American Helicopter Society International, Phoenix, AZ, USA, 6–8 May 2003 .
20. Donaldson, C.; Bilanin, A.J. *Vortex Wakes of Conventional Aircraft*; AGARD: Neuilly sur Seine, France, 1975.
21. Landgrebe, A.J. The Wake Geometry of a Hovering Helicopter Rotor and Its Influence on Rotor Performance. *J. Am. Helicopter Soc.* **1972**, *17*, 3–15. [CrossRef]
22. Quagliarella, D. *Aerodynamic Shape Design Using Evolutionary Computation: A Tutorial with Examples and Case Studies*; American Institute of Aeronautics and Astronautics (AIAA): Reston, VA, USA, 2014; pp. 529–581.

23. Sobol, I.M. Distribution of points in a cube and approximate evaluation of integrals. *Zh. Vych. Mat. Mat. Fiz.* **1967**, *7*, 784–802. (In Russian); *USSR Comput. Maths. Math. Phys.* **1967**, *7*, 86–112. (In English) [CrossRef]
24. Casalino, D. An advanced time approach for acoustic analogy predictions. *J. Sound Vib.* **2003**, *261* , 583–612. [CrossRef]
25. Casalino, D.; Barbarino, M.; Visingardi, A. Simulation of Helicopter Community Noise in Complex Urban Geometry. *AIAA J.* **2011**, *49*, 1614–1624. [CrossRef]
26. Farassat, F. Linear Acoustic Formulas for Calculation of Rotating Blade Noise. *AIAA J.* **1981**, *19*, 1122–1130. [CrossRef]
27. De Gregorio, F.; Rossignol, K.S.; Ceglia, G.; Yin, J. Aerodynamic and acoustic investigations of rotor-rotor wake interaction. In Proceedings of the 21st International Symposium on the Application of Laser and Imaging Techniques to Fluid Mechanics, Lisbon, Portugal, 8–11 July 2024; Volume 21, pp. 1–27. [CrossRef]
28. Graftieaux, L.; Michard, M.; Grosjean, N. Combining PIV, POD and vortex identification algorithms for the study of unsteady turbulent swirling flows. *Meas. Sci. Technol.* **2001**, *12*, 1422. [CrossRef]
29. De Gregorio, F.; Visingardi, A.; Iuso, G. An Experimental-Numerical Investigation of the Wake Structure of a Hovering Rotor by PIV Combined with a Γ_2 Vortex Detection Criterion. *Energies* **2021**, *14*, 2613 . [CrossRef]
30. Leishman, J.G. *Principles of Helicopter Aerodynamics*; Cambridge University Press: New York, NY, USA, 2000; Chapter 10.
31. Omori, K.; Kojima, H.; Kakani, R.; Slavit, D.H.; Blaugrund, S.M. Acoustic characteristics of rough voice: Subharmonics. *J. Voice* **1997**, *11*, 40–47. [CrossRef]
32. Gwak, D.Y.; Yoon, K.; Seong, Y.; Lee, S. Application of subharmonics for active sound design of electric vehicles. *J. Acoust. Soc. Am.* **2014**, *136*, EL391–EL397. [CrossRef]